1 # Supplementary Information

2

3 **High-performance trimethylamine gas sensors based on defect-**

4 **engineering MOFs-derived ZnO nanoclusters with tunable surface**

5 **oxygen vacancy**

6

7 Shaoyuan Yu, Jingshi Dong, He Wang, Sirui Li, Hang Zhu* and Tianye Yang*
8 School of Mechanical and Aerospace Engineering, Jilin University, Changchun, 130022, People's
9 Republic of China
10 *Corresponding authors. *E-mail* addresses: hangzhu@jlu.edu.cn and yangty@jlu.edu.cn

11
12
13
14
15
16
17
18
19
20
21
22
23
24
25
26
27
28
29
30
31
32
33
34
35
36

37 **1.1 Schematic illustration of DE MOFs-derived ZnO nanoclusters**
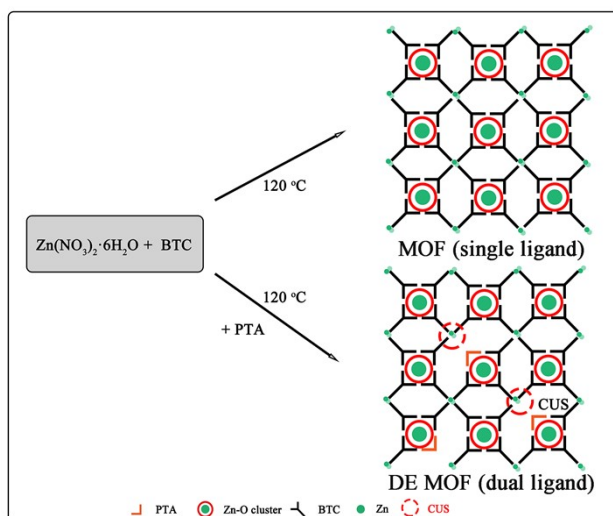

Fig. S1. Schematic illustration structure of single ligand MOF and DE MOF, respectively.

38   In this paper, we want to obtain different oxygen vacancies through design rational structure of DE Zn-MOF

39 precursors and subsequent annealed process. This is because the structure of MOFs is easily controlled by mixing

40 different mental ions and organic acids. DE Zn-MOF with CUSs (coordinate unsaturated Zn^{2+} ions) is obtained by

41 competitive coordination of two organic acids with Zn^{2+}, as shown in Fig. S1.
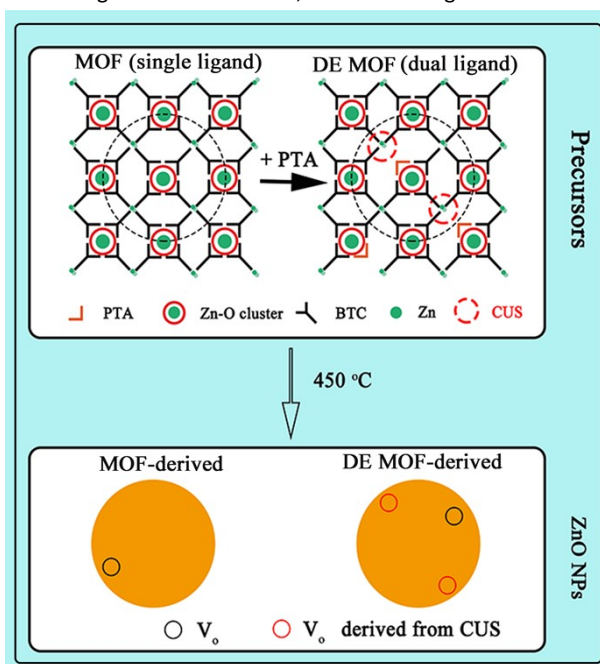

Fig. S2. The transformation process diagram of MOFs precursor to ZnO NPs at 450 °C.

42   After the annealing process, the lack of coordination oxygen atoms of the CUSs in DE Zn-MOF are transformed

43 to oxygen vacancies, as shown in Fig. S2.

44 **1.2. Fabrication of sensors**

45   The sensor element consists of a ceramic substrate and a ZnO-based sensing material, as shown in Fig. S3.

46 The ceramic substrate is sintered from alumina. Measuring and heating electrodes were printed with gold and

47 ruthenium on the upper and lower surfaces respectively. In the first step, an appropriate amount of as-synthesized

48 powder was poured into a mortar and ground into a homogeneous paste with the assistance of a small amount of

49 deionized water. It was then coated on the interdigital electrode on the upper surface of the ceramic substrate
50 with a brush. After the film was dried, the Pt leads on the base were welded together with the base. For the stability
51 of the sensor, the heating electrode was energized to indirectly heat the prefabricated film. SL1-SL5 sensors were
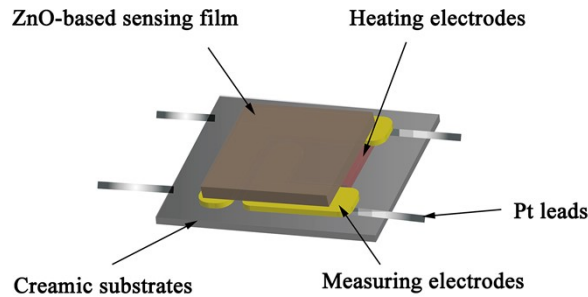52 all burn-in for 10 h at 180 $^{\circ}$C.

Fig. S3. Schematic illustration structure of SL1-SL5 sensors.

53 **1.3. Sensor performance test**

54 The resistance change process of the gas-sensitive element under different gas conditions is recorded and
55 analyzed using the CGS-8 Intelligent Gas Sensor Analysis System. The steady resistance value (R_a) of the sensor in
56 the air bottle and the steady resistance value (R_g) in the test gas bottle are collected under different operating
57 temperature conditions (25 ± 5%RH, 20 ± 3 $^{\circ}$C), and finally the sensor is moved back to the air bottle. The response
58 value is defined as shown in Eq. S1, and the response and recovery times are the time required for the sensor to
59 reach 90% response value in the test bottle and to return to 90% stable resistance value in the air bottle,
60 respectively. The static gas distribution method is taken to obtain the concentration of TMA. The specific volume
61 of TMA solution required for a particular concentration was calculated by Eq. S2 and then transferred to a 1L bottle
62 using a syringe for subsequent experiments. The gas in the bottle was allowed to evaporate for 30 min and then
63 tested.

$$S = R_a/R_g \tag{S1}$$
$$C = 22.4 \times d \times p \times V_1 \times 1000/M \times V_2 \tag{S2}$$

64 where, C is the gas concentration (ppm), d is the required gas volume fraction, ρ, V1, V2, M are the solution
65 density (g/mL), the volume of the liquid (μL) and the volume of the test container (L) as well as the molecular
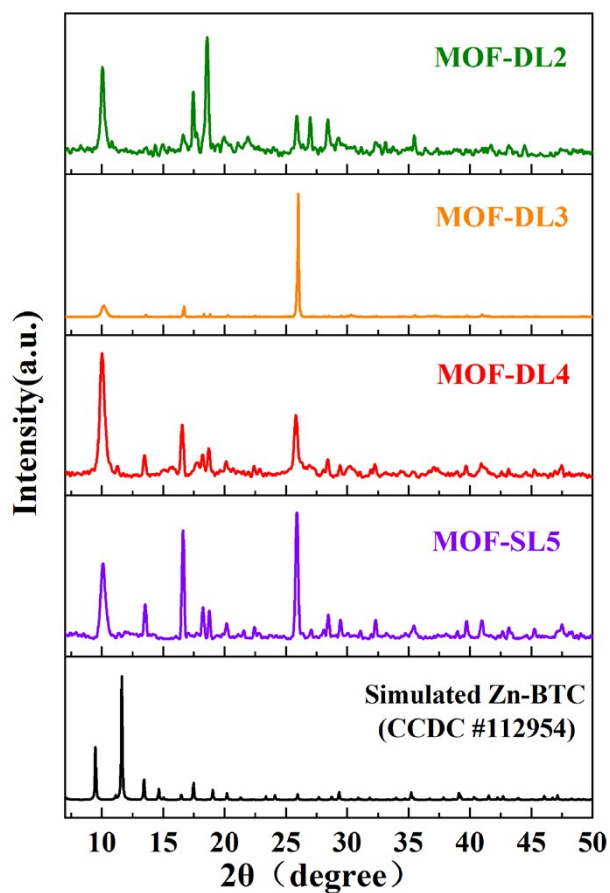66 weight of solution (g/mol).

1.4. PXRD

Fig. S4. The PXRD patterns of MOF-DL2, MOF-DL3, MOF-DL4 and MOF-SL5 compare with simulated Zn-BTC patterns (CCDC #112954).

Table. S1 Calculated interplanar distance d values.

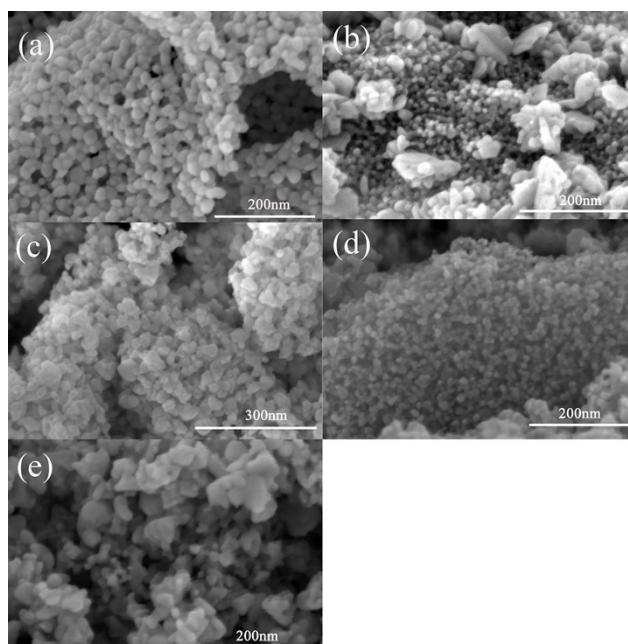| Samples	(100)		(002)		(101)	
	2θ (degree)	d (Å)	2θ (degree)	d (Å)	2θ (degree)	d (Å)
SL1	31.83	2.809	34.45	2.601	36.29	2.473
DL2	31.76	2.815	34.36	2.608	36.20	2.479
DL3	31.75	2.816	34.42	2.603	36.26	2.476
DL4	31.80	2.811	34.40	2.605	36.28	2.474
SL5	31.83	2.809	34.45	2.601	36.33	2.471

1.5. SEM

Fig. S5. (a-e) SEM images of SL1-SL5 at 200-300 nm resolution.
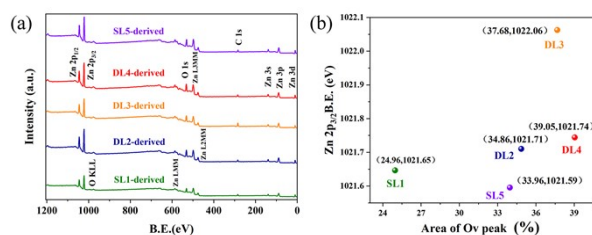
1.6. XPS

Fig. S6. (a) The XPS survey spectra (0-1200 eV) of SL1-SL5. (b) The area of Ov peak and binding energies of Zn $2p_{3/2}$ of SL1-SL5.

Table S2. Atom ratios of O/Zn on the surface of SL1- SL5 was calculated from XPS survey spectra

samples	SL1	DL2	DL3	DL4	SL5
O	42.3%	39.62%	42.34%	39.87%	40.34%
Zn	57.7%	60.38%	57.66%	60.13%	59.66%

(Standard ZnO stoichiometry ratios =1:1)

DL3 has high O/Zn ratios and an unusually high Ov peak area of 37.68%. It can be observed in Fig. 5f that the BE of Zn 2p3/2 was shifted in five samples. Figure S6b shows the corresponding Ov peak areas and BE of Zn $2p_{3/2}$ for the five samples. It is found that DL3 has the highest BE of the Zn $2p_{3/2}$ peak and is ~ 0.47 eV larger than DL4. Since electrons have a shielding effect on the nucleus, higher binding energy of the Zn $2p_{3/2}$ orbitals indicates that the zinc atoms near the surface have fewer electrons around them. This implies that some of the electrons of DL3 are bound by the oxygen vacancies of DL3, leading to the possibility that the oxygen vacancies exhibit a lower valence state. In contrast, the oxygen vacancies in the surface layers of SL1, DL2, DL4 and SL5 are more likely to be present in the V_o^{2+} state.
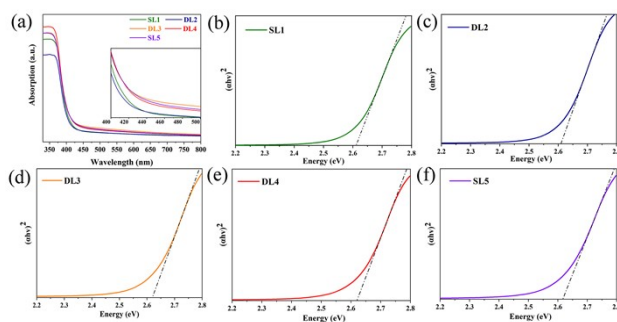
79 **1.7. UV-vis**

Fig. S7. (a) The plot of UV-vis absorption spectrum of SL1-SL5. (b-f) The plot of $(\alpha h\nu)^2$ vs. photon energy ($h\nu$) of SL1-SL5, respectively.
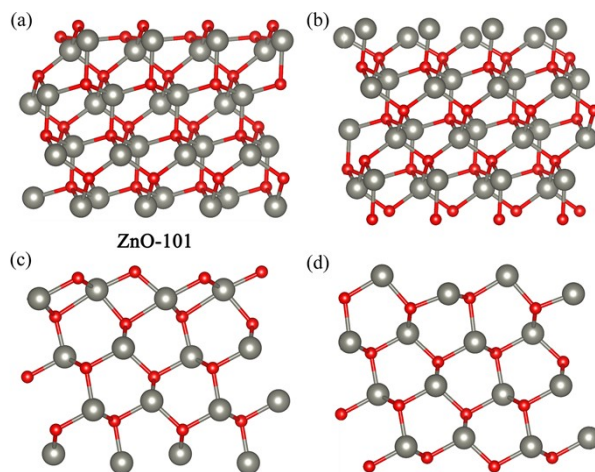
80 **1.8. DFT**

Fig. S8. (a-d) Optimization models for (101) faces of ZnO with the hexagonal wurtzite structure and the surface energies of are 2.37 J/m^2, 3.63 J/m^2, 3.49 J/m^2 and 2.51 J/m^2, respectively.

Table. S3 Adsorption energy of TMA molecules on different surfaces.

Surface	Adsorption Energy
ZnO-101	-1.28eV
ZnO-101-v	-1.79eV

81